Brachytherapy seed reconstruction with joint-encoded C-arm single-axis rotation and motion compensation

Ehsan Dehghan[a], Ameet K. Jain[b], Mehdi Moradi[c], Xu Wen[c], W. James Morris[d], Septimiu E. Salcudean[c], Gabor Fichtinger[a,*]

[a] School of Computing, Queen's University, Kingston, ON, Canada
[b] Philips Research North America, Briarcliff, NY, USA
[c] Electrical and Computer Engineering Department, The University of British Columbia, Vancouver, BC, Canada
[d] Vancouver Cancer Centre, British Columbia Cancer Agency, Vancouver, BC, Canada

ARTICLE INFO

ABSTRACT

C-arm fluoroscopy images are frequently used for qualitative assessment of prostate brachytherapy. Three-dimensional seed reconstruction from C-arm images is necessary for intraoperative dosimetry and quantitative assessment. Seed reconstruction requires accurately known C-arm poses. We propose to measure the C-arm rotation angles and computationally compensate for inevitable C-arm motion to compute the pose. We compensate the translational motions of a C-arm, such as oscillation, sagging and wheel motion using a three-level optimization algorithm and obviate the need for full pose tracking using external trackers or fiducials. We validated our approach on simulated and 100 clinical data sets from 10 patients and gained on average, a seed matching rate of 98.5%, projection error of 0.33 mm (STD = 0.21 mm) and computation time of 19.8 s per patient, which must be considered as clinically excellent results. We also show that without motion compensation the reconstruction is likely to fail.

1. Introduction

Prostate cancer continues to be the leading cancer among men in the United States with an estimated occurrence of 217,730 new cases in 2010 (Jemal et al., 2010). Low dose rate brachytherapy (henceforth, brachytherapy) is an effective treatment for localized prostate cancer that can achieve excellent outcomes (Blasko et al., 2002; Morris et al., 2009a,b). Brachytherapy entails permanent placement of radioactive capsules (seeds) of ^{125}I or ^{103}Pd inside the prostate and periprostatic tissue to kill the cancer with radiation. Brachytherapy seeds are as small as a grain of rice, approximately 4.5 mm long and 0.8 mm in diameter. The success of the procedure directly depends on the accuracy of seed placement to deliver sufficient dose to eradicate the cancer while sparing the urethra and rectum. The seed positions are preplanned to tailor the dose to the patient's anatomy. Generally 40–130 seeds are implanted depending on the type of the seeds and the volume of the prostate. During 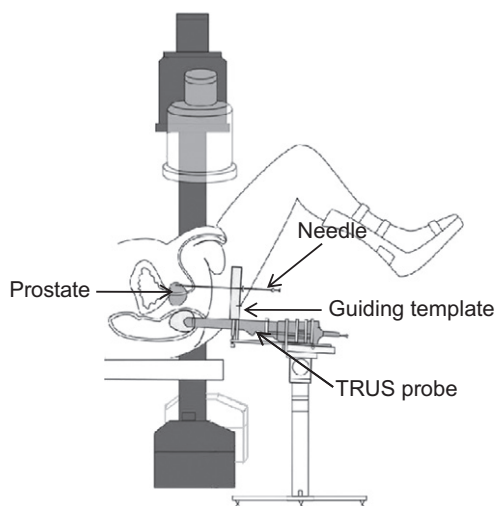the procedure, the physician delivers the seeds using needles that pass through a guiding template, under real-time visual guidance from transrectal ultrasound (TRUS) (Prestidge et al., 1998). The guiding template confines the needles to move in parallel to the long axis of the probe. C-arm fluoroscopy images are frequently taken during the procedure to qualitatively assess the implant (see Fig. 1).

Accurate execution of the plan is extremely difficult due to prostate displacement and deformation (Lagerburg et al., 2005), needle bending, prostate swelling (Yamada et al., 2003) and, system calibration and human errors. As a result, seed misplacements are still common and may lead to under-dosed regions that necessitate repeated treatment, or over-dosed regions which result in complications, such as rectal ulceration, urinary incontinence and sexual dysfunction. Intraoperative dosimetry and planning methods were introduced to reduce the errors and increase the treatment quality (Nag et al., 2001; Orio et al., 2007; Polo et al., 2010). These methods intermittently calculate the delivered dose during the procedure and modify the insertion plan, in real-time, to compensate for possible errors.

In order to calculate the dose distribution, the position of the implanted seeds, registered to the prostate anatomy, should be known. Ultrasound imaging provides sufficient soft tissue contrast to delineate the prostate; however, despite the efforts (Han et al., 2003; Holmes and Robb, 2004; Feleppa et al., 2002; McAleavey et al., 2003; Mitri et al., 2004; Ding et al., 2006; Wei et al., 2006; Wen et al., 2010), robust seed segmentation in ultrasound is not

Fig. 1. Brachytherapy procedure. The needle passes through the guiding template in parallel to the long axis of the transrectal probe. The C-arm rotates around the craniocaudal axis of the patient to acquire images. This figure is reproduced from Lee et al. (2009) with permission form the authors.

yet possible (up to 25% of seeds can be hidden even after careful manual segmentation in B-mode images (Han et al., 2003)). X-ray fluoroscopy images provide excellent seed visualization. However, fluoroscopy images do not provide sufficient soft tissue contrast to segment the prostate boundaries. Fluoroscopy-ultrasound fusion can provide a solution for real-time intraoperative dosimetry and has been extensively studied (French et al., 2005; Su et al., 2006; Orio et al., 2007; Tutar et al., 2008; Fallavollita et al., 2010). In this scenario, during and/or immediately after the brachytherapy procedure, several C-arm images are taken from different angles and segmented for seed centroids. Then, the seeds are localized in 3D space using the segmented images. By registration of these seeds to the prostate anatomy localized in ultrasound, the delivered dose to the prostate can be calculated. Upon observation of large seed misplacements or cold spots, the physician can modify the plan and implant new seeds. Reconstruction accuracy and speed are vital for intraoperative dosimetry using fluoroscopy-ultrasound fusion.

Three-dimensional seed reconstruction has been widely investigated in the literature (Amols and Rosen, 1981; Tubic et al., 2001a; Todor et al., 2002; Tutar et al., 2003; Su et al., 2004; Narayanan et al., 2004; Lam et al., 2004; Jain et al., 2005b; Kon et al., 2006; Brunet-Benkhoucha et al., 2009; Lee et al., 2009; Lee et al., 2011). In order to successfully reconstruct the seed positions in 3D, three major problems must be solved.

(1) *C-arm calibration*: For an accurate reconstruction, C-arm intrinsic parameters, such as image resolution, image center, source to center distance and focal length should be known (Navab et al., 1996; Brack et al., 1996; Jain et al., 2005a).
(2) *Seed matching*: After segmentation of the 2D coordinates of seed projections in the C-arm images, a seed matching problem should be solved to assign each seed projection in one image to the corresponding seed projections in the other images (see Fig. 2 for an example). Since the seed matching is not known, seed reconstruction using two C-arm images leads to an ambiguity that can be resolved using a third image. Therefore, at least three images are required for seed localization in 3D space. Seed matching has been solved using various methods, such as simulated annealing (Tubic et al., 2001a), heuristic rules (Todor et al., 2002) and the Hungarian algorithm (Jain et al., 2005b). Hidden or overlap-
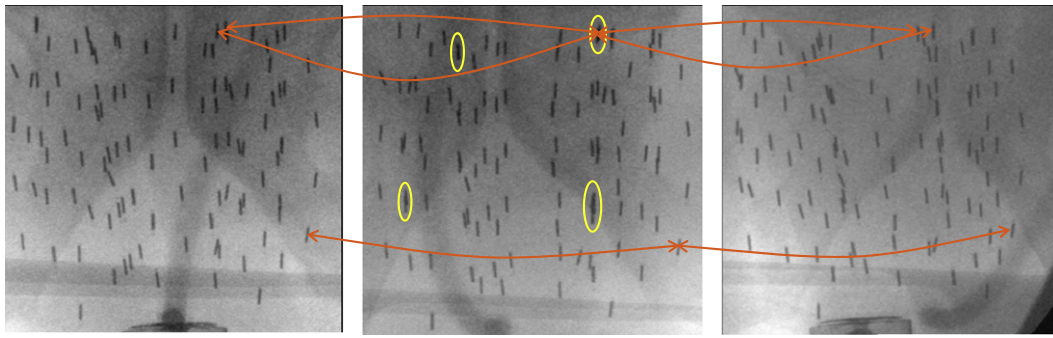
ping seed projections are common in projection images and result in incomplete data sets that further complicate the seed matching problem (see Fig. 2). The hidden seed problem has been tackled using different approaches, such as pseudo-seed-matching (Narayanan et al., 2004), adaptive grouping (Su et al., 2004), Hough trajectories (Lam et al., 2004), an extension to the Hungarian algorithm using network flow (Kon et al., 2006) and dimensionality reduced linear programing (Lee et al., 2011). It should be noted that tomosynthesis-based reconstruction methods have been proposed that solve the matching problem automatically (Tutar et al., 2003; Brunet-Benkhoucha et al., 2009; Lee et al., 2009). However, these methods generally need a larger number of images.

Jain et al. showed that seed matching is equivalent to a network flow problem which is NP-Hard (Jain et al., 2005b). However, they proposed a pseudo-polynomial yet practical solution for seed matching from three images by mapping the original tripartite problem into three bipartite ones that could be solved using the Hungarian algorithm. Jain's method was abbreviated as MARSHAL (Jain et al., 2005b). The original MARSHAL assumed complete data sets; however, it was later extended to address the hidden seed problem (Kon et al., 2006) (the extended method was abbreviated as XMARSHAL). This algorithm demonstrated clinically acceptable reconstruction rates and time performance on simulated and phantom data, and has been clinically tested (Song et al., 2011; Jain et al., in press). We will discuss XMARSHAL in more details in Section 2.1 as it runs in the core of our algorithm.
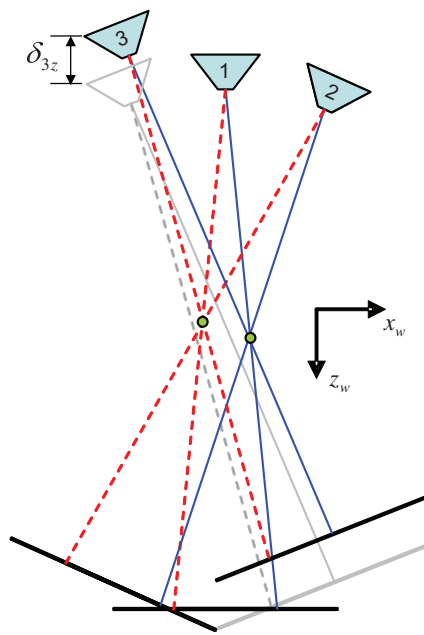
(3) *Pose recovery*: Seed matching and reconstruction are performed using known C-arm poses that provide the relative positions of the C-arm images in 3D space. The C-arm pose is generally recovered using radio-opaque fiducials or beads (Navab et al., 1996; Brack et al., 1996; Zhang et al., 2004; Jain et al., 2005a), or obtained from electromagnetic and optical trackers (Peters and Cleary, 2008). Fiducials may interfere with the image of the anatomy, require segmentation and can limit the working volume. Auxiliary trackers are expensive, need calibration, optical trackers require line of sight, electromagnetic trackers are sensitive to interference and hence, further complicate the intervention. It has been suggested to use the implanted seeds as fiducials to compensate for C-arm pose computation errors (Tubic et al., 2001a; Jain and Fichtinger, 2006; Lee et al., 2009). However, a good initial measurement of the pose is required and is usually obtained by using fiducials and trackers. Pose recovery without a fiducial or tracker can significantly ease the reconstruction process and consequently facilitate the transition of seed reconstruction algorithms from research laboratories to medical practice. In this work, we introduce a method to estimate the pose using sole measurement of rotation angles and computationally compensate for the pose computation errors without fiducials or external trackers.

It is common practice in brachytherapy to acquire several images by rotating the C-arm around the patient. Usually, the rotation axis is approximately aligned with the patient's craniocaudal axis. In ideal cases, joint angle measurements can yield an accurate pose of the C-arm. However, C-arm movements, such as oscillation, sagging and wheel motion are significant and prevent accurate pose recovery based solely on joint angle measurements (see Fig. 3). If uncompensated, these C-arm motions can lead to severe pose computation errors and reconstruction failure.

In this paper, we prove that in the typical case of a C-arm rotated around a single axis within a small angle span, C-arm angle

Fig. 2. Three C-arm images taken at different angles. The figure at the middle shows several hidden and overlapping seeds. Three seed matchings are shown using arrows. The seeds move along an almost horizontal line through the images.

Fig. 3. Initial (gray) and correct C-arm pose (color) for the third C-arm. Translational error along the up–down direction is only added to C-arm 3. The reconstructed seeds are shown after motion compensation. (For interpretation of the references to color in this figure legend, the reader is referred to the web version of this article.)

measurements augmented with a computational method to compensate for C-arm motions suffice for a clinically reliable and accurate seed reconstruction. However, without such a motion compensation algorithm, the reconstruction is prone to failure. We employ joint encoders or digital protractors to measure the rotation angles. The novelty of this work is in the introduction of an effective motion compensation method that obviates the need for full pose tracking using external fiducials or trackers. Considering the simplicity of the implementation, high reconstruction accuracy and favorable computational speed, this algorithm is suitable for clinical translation. The underlying idea and limited preliminary data was presented at a recent conference (Dehghan et al., 2010). This manuscript provides a more detailed description of the methodology and performance analysis on 100 clinical data sets.

This paper is organized as follows. The algorithms for seed matching and motion compensation are explained in Section 2. Numerical simulation, phantom and clinical results are presented in Section 3, followed by discussion in Section 4. The conclusions are drawn and the future work is outlined in Section 5.

2. Methods

We propose an iterative three-level algorithm that takes advantage of the constrained movement of a C-arm during coplanar imaging, compensates for its major translational motions using reconstructed seeds and, in turn, significantly increases the likelihood of finding the correct matching solution in a clinically acceptable time. We compensate for C-arm motions that are mostly translational. That is an approximation of the C-arm motion pattern. However, as our results prove, it is sufficient for successful reconstructions. Our motion compensation algorithm can be used with any seed matching algorithm. For seed matching and reconstruction, we employ XMARSHAL (Kon et al., 2006) that is capable of solving the matching problem in the presence of hidden seeds with low computational cost. For the sake of completeness we briefly outline this method in Section 2.1. As mentioned, tomosynthesis-based reconstruction methods do not require a matching algorithm. However, they suffer from lack of accurate C-arm pose too. Therefore, C-arm motion compensation framework applies to them as well.

2.1. Seed reconstruction using XMARSHAL

Assume that three C-arm images of an implant with N seeds are available and $N_i, i \in \{1,2,3\}$ seed projections are segmented in each image. In this case, the seed matching problem in the presence of hidden seeds can be written as the following optimization problem:

$$m^*_{ijk} = \arg\min_{m_{ijk}} \sum_{i=1}^{N_1} \sum_{j=1}^{N_2} \sum_{k=1}^{N_3} c_{ijk} m_{ijk}, \tag{1}$$

$$\text{s.t.} \begin{cases} \sum_{j=1}^{N_2} \sum_{k=1}^{N_3} m_{ijk} \geqslant 1, & \forall i \\ \sum_{i=1}^{N_1} \sum_{k=1}^{N_3} m_{ijk} \geqslant 1, & \forall j \\ \sum_{i=1}^{N_1} \sum_{j=1}^{N_2} m_{ijk} \geqslant 1, & \forall k \\ \sum_{i=1}^{N_1} \sum_{j=1}^{N_2} \sum_{k=1}^{N_3} m_{ijk} = N, \\ m_{ijk} \in \{0,1\}, \end{cases}$$

where for each $i \in \{1,\dots,N_1\}, j \in \{1,\dots,N_2\}$ and $k \in \{1,\dots,N_3\}$, c_{ijk} is the cost of matching seed projections p_i^1, p_j^2 and p_k^3 from the first, second and third images, respectively, and m_{ijk} is a binary variable showing the correctness of such a match. The constraints in (1) ensure reconstruction of N seeds while taking the hidden seeds into account.

Assume three rays emanating from each of these seed projections p_i^1, p_j^2 and p_k^3 to its corresponding X-ray source in 3D space. The point with the minimum average distance from these lines is considered as their symbolic intersection. We define the average distance of the symbolic intersection from these lines as their symbolic distance. If we project the symbolic intersection on each image, the summation of the distances between this projection and the corresponding seed projection on each image is considered as the matching cost (c_{ijk}) (Jain et al., 2005b).

Eq. (1) is a weighted-tripartite matching problem that is equivalent to an NP-Hard combinatorial optimization (Jain et al., 2005b) with an exponential complexity. An approximate low computational cost solution to this problem was proposed by Jain et al. by projecting the tripartite matching problem into three bipartite problems (Jain et al., 2005b). In this solution, seed projections p_i^1 and p_j^2 can be matched (with a cost c_{ij}) only if they have a low cost counterpart in the third image. In this method:

$$c_{ij} = \min_k c_{ijk}, \forall k. \tag{2}$$

This is based on the observation that although low c_{ij}, c_{jk} and c_{ki} do not guarantee a low c_{ijk}, a low c_{ijk} guarantees c_{ij}, c_{jk} and c_{ki} to be low.

This solution resembles a network-flow optimization problem in which each seed projection in an image is represented by a node (Jain et al., 2005b; Kon et al., 2006). The matching between two seed projections is represented by a link that flows between them with a cost equal to the matching cost c_{ij}. This network flow problem was extended in Kon et al. (2006) to address the hidden seeds problem. This problem can be solved using a cycle canceling algorithm in practically $O(N^3)$ times (Kon et al., 2006), producing clinically excellent matching.

Given the correct matching and the C-arm poses, the 3D position of the seeds with minimized reconstruction cost is calculated as:

$$s_i = \left[\sum_{j=1}^{3} \left(I - v_{ij} v_{ij}' \right) \right]^{-1} \sum_{j=1}^{3} \left(I - v_{ij} v_{ij}' \right) q_j, \tag{3}$$
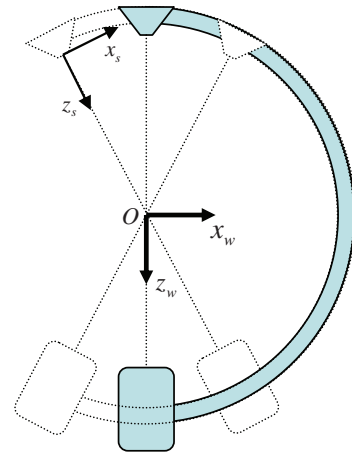$$i \in \{1, \ldots, N\},$$

where s_i is the position of the ith seed, q_j is the position of the X-ray source corresponding to the jth image, v_{ij} is the unit vector along the lines L_{ij} that connect the projection of seed i on image j to q_j and I is a 3×3 identity matrix. The reconstruction cost for seed i is defined as the symbolic distance between lines L_{i1}, L_{i2} and L_{i3}.

2.2. Motion compensation

Let us assume a world coordinate system $Ox_w y_w z_w$ centered at the center of rotation of the C-arm and a source coordinate system $Ox_s y_s z_s$ centered at the X-ray source as shown in Fig. 4. The pose of the C-arm is defined by a transformation matrix $^s\mathbf{T}_w$ from the world to the source coordinate system as:

$$^s\mathbf{T}_w = \begin{bmatrix} ^s\mathbf{R}_w & -^s\mathbf{R}_w \delta + \begin{bmatrix} 0 \\ 0 \\ l \end{bmatrix} \\ \mathbf{0}' & 1 \end{bmatrix}, \tag{4}$$

where $^s\mathbf{R}_w$ is the rotation matrix from the world to the source coordinate frame, l is the distance from the source to the center of rotation and $\delta = [\delta_x \ \delta_y \ \delta_z]'$ is the translational motion of the C-arm caused by oscillation, sagging and wheel motion (see Fig. 3). We can initialize a pose computation by measuring the C-arm rotation angles – which define $^s\mathbf{R}_w$ – and setting the unknown δ equal to zero. Assuming $\delta = \mathbf{0}$ causes error in the pose computation and sub-
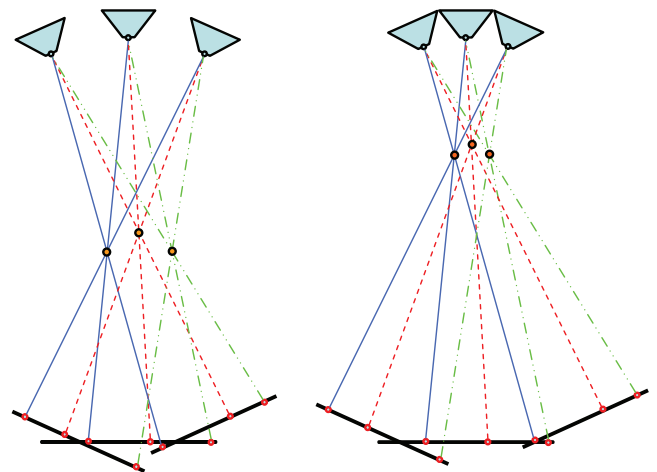

Fig. 4. A C-arm rotating around its primary axis (PA) in a single plane. The angle around the secondary axis (SA) is fixed. The world coordinate system $Ox_w y_w z_w$ is centered at the center of rotation. The source coordinate system $Ox_s y_s z_s$ is centered at the source.

sequent unsuccessful seed reconstruction. Therefore, we should compensate for this error and improve our pose computation.

An iterative scheme can be implemented where the reconstructed seeds with given C-arm poses are used to improve the pose recovery and subsequently enhance the seed reconstruction results. Such iterative schemes were suggested in the literature to compensate for the rotational and translational pose errors (6 DOFs) (Tubic et al., 2001a; Jain and Fichtinger, 2006). It is known that such a problem can be solved up to an unknown scale (Jain and Fichtinger, 2006). This means that the reconstructed seed cloud can arbitrarily shrink or expand. As it is shown in Fig. 5, the X-ray images, C-arm intrinsic parameters, seed matching and relative C-arm rotations are identical between two sets of reconstruction solutions; however, the scaled relative translations result in a scaled seed cloud.

We demonstrate that by making realistic and practical assumptions in accordance with clinical protocols, motion compensation can be reduced to 2 DOFs for mobile C-arms used in brachytherapy. This approach eliminates the scaling problem and results in a clinically adequate implant reconstruction and computational time small enough to be carried out intraoperatively. Pose error com-

Fig. 5. The scaling effect results from 3 DOF translational motion of the C-arm. The X-ray images, C-arm relative rotations and C-arm intrinsic parameters are identical between the left and right reconstructions. Seed matching solution is independent of the scaling factor.

pensation for 2 DOFs requires less complicated algorithms (compare to 6 DOFs) and thus is computationally faster.

We make the following assumptions:

1. The C-arm images are acquired by rotation of a C-arm around its primary axis (PA) in a small angle span, while the angle around the secondary axis (SA) is fixed (see Fig. 4).
2. C-arm rotation angles are measured.
3. The intrinsic parameters are known and do not change during rotation of the C-arm.
4. 2D coordinates of seed projections are available via manual or automatic segmentation.
5. Most significant C-arm motions are of translational nature, confined to the $Oy_w z_w$ plane – the motion along x_w is negligible ($\delta_{ix} = 0, i \in \{1, 2, 3\}$).

As mentioned before, acquiring images by rotating the C-arm around its PA while the angle around SA is fixed is common practice in brachytherapy. The rotation span around PA is usually limited to approximately ±15° due to collision of the C-arm with the operating table, brachytherapy stand or patient's legs. Mobile C-arms are available that employ a fixed axis of rotation and are equipped or can be easily retrofitted with joint encoders (Grzeda and Fichtinger, 2010).

Limited rotation span in a clinical setting results in an insignificant change in the calibration parameters, such as focal length, image center and source to center distance. Image resolution is considered as constant over the lifetime of the device. It has been shown that in such situations recalibration for each C-arm pose is not necessary, because small changes in the calibration parameters do not significantly alter the relative positions of the reconstructed seeds (Jain et al., 2007). It should be noted that we are interested in the relative position of the seeds as the seed cloud as a whole should later be registered to the prostate anatomy.

In this work we relied on manual segmentation to identify the seed centroids. Since XMARSHAL is capable of addressing the hidden seeds problem, it is not required to identify all the implanted but hidden seeds in every image. The effects of hidden seed percentage and seed segmentation error on the performance of XMARSHAL are discussed in Kon et al. (2006).

The last assumption is the cornerstone of our motion compensation algorithm. The most likely source of pose computation error is the oscillation of the C-arm, which is mostly up-down (along the z_w axis) since the C-arm is connected to the base as a cantilever. Our observations confirm this assumption that the C-arm primary motion is in the up-down direction due to oscillation and C-arm weight. The motion in the other two directions are much smaller; however, are not always insignificant. As a result, C-arm pose computation error along z_w is more significant compared to the inaccuracies in the other two directions.

The proposed motion compensation algorithm initializes the C-arm pose using measured joint angles as shown in Fig. 3 and compensates for the inevitable translational motions by finding the optimal translational adjustments (offsets) δ for each source position, by solving the following problem:

$$\left(m_{ijk}^*, \delta_n^*\right) = \arg\min_{x_{ijk}, \delta_n} \sum_{i=1}^{N_1} \sum_{j=1}^{N_2} \sum_{k=1}^{N_3} c_{ijk}(\delta_n) m_{ijk}, \qquad (5)$$

$$n \in \{1, 2, 3\},$$

subject to the constraints of (1). In order to minimize the scaling effects, we restrict the offsets to be in the $Oy_w z_w$ plane – based on our assumption - and introduce a three-level optimization method to identify them.

2.2.1. First-level optimization

At the first level, the algorithm finds a few matching seed projections in the images to calculate an initial offset estimate with very low computational cost. Since the fluoroscopy images are taken with the rotation of the C-arm around its PA, the seed projections follow almost horizontal lines in the images. Therefore, a seed at the top or bottom of one image is more likely located at the top or bottom of the other images (for example see Fig. 2). Based on this observation, the algorithm automatically selects n seed projections from the top (seeds with maximum ordinate values in the 2D image coordinate system) and n seed projections from the bottom of each image (seeds with minimum ordinate values in the 2D image coordinate system) and solves the matching problem for them, using the initial estimates of the C-arm poses from joint angle readings. Since the selected $2n$ seed projections from one image do not necessarily correspond to the selected $2n$ seed projections in the other images (these $6n$ seed projections may belong to more than $2n$ seeds in 3D), some of the reconstructed seeds have a high reconstruction cost, are erroneously matched, and cannot be used to improve the pose recovery. Therefore, the algorithm selects a subset of $p < n$ reconstructed seeds from the top and p reconstructed seeds from the bottom of the $2n$ reconstructed seeds with the best reconstruction costs for pose recovery. We use $n = 5$ and $p = 2$. In order to estimate the C-arm motion, we assume that the position of the C-arm source corresponding to the first image (henceforth, the first source position) in 3D space is fixed ($\delta_1 = \mathbf{0}$) and optimize the position of the C-arm sources corresponding to the second and third images (henceforth, the second and third source positions) in the $Oy_w z_w$ plane to minimize the reconstruction cost for the selected $2p$ seeds. The seed matching and motion estimation are iteratively performed until there is no change in the seed matching solution.

Since a small number of seed projections are used at this level, the matching problem can be solved extremely quickly using XMARSHAL. With a given matching, 2D offsets for the second and third C-arm source positions can be found by solving a set of linear equations. These equations are derived in (A.6)–(A.15).

2.2.2. Second-level optimization

In this step, the C-arm source positions are initialized in 3D space using the optimal offset values from the first level. Then, the matching problem is solved for all seed projections and the seeds are reconstructed. The C-arm source positions are optimized in 3D space to minimize the average reconstruction cost while the seeds are fixed in space. The matching and source position optimizations are iteratively solved until the reconstruction cost or its change between two iterations is smaller than a predefined threshold. The thresholds were empirically assigned as <0.1 mm for the former and <0.1% for the latter.

The new position of the jth X-ray source at iteration $k + 1$ is calculated as:

$$q_j^{k+1} = \left[\sum_{i=1}^{N} (I - v_{ij} v_{ij}')\right]^{-1} \sum_{i=1}^{N} (I - v_{ij} v_{ij}') s_i^k, \qquad (6)$$

where s_i^k is the position of the ith seed at iteration k.

Since we employ a 3D optimization at this level, the reconstructed seed cloud may significantly shrink or expand (see Fig. 5). However, optimization in 3D increases the likelihood of finding the correct matching which is independent of the scaling factor. Therefore, we take advantage of 3D optimization at this level, find the correct matching and remove the scaling effects at the next level.

2.2.3. Third-level optimization

At this step, we assume that the correct matching solution is available from the second-level optimization. However, the seed cloud may be scaled due to 3D motion compensation. Therefore, once more, we assume that the C-arm motion along x_w is negligible and optimize for 2D C-arm motion. The C-arm source positions are initialized using the joint angle readings. The first source is fixed in space. Next, 2D offsets of the second and third source positions are optimized to minimize the reconstruction cost with the given matching. Similar to the first level, the 3D seed positions and 2D offsets for the sources have a closed form solution, the equations for which are derived in (A.6)–(A.15). The three steps of the algorithm are shown in Fig. 6.

3. Results

3.1. Simulations

First, the motion compensation algorithm was tested on simulated data. We synthesized four seed clouds based on realistic dosimetry plans of four patients with 100, 102, 108 and 130 seeds. Seed images were synthesized by rotation of the C-arm around the PA at 0°, ±5° and ±10°, while the SA angles were kept constant at 180°. The intrinsic parameters of a GE OEC® 9800 device were used as the intrinsic parameters of the C-arm in the simulations. The seeds were reconstructed using every possible combination of three images out of five. In order to investigate the performance of our motion compensation algorithm, translational and rotational pose errors were added to one of the C-arm source-image pairs. The added errors were 0–10 mm along x_w and y_w, 0–20 mm along z_w with steps of 1 mm and 0–3° around SA and PA with steps of 0.5°. The effects of these errors were simulated independently, as only one error was introduced at each simulation. During image synthesis, hidden seed projections were created by merging the seed projections that were close to each other. There were on average 1.6 hidden seeds per image, with a maximum of 14.

The reconstructed seeds were compared against the ground truth after a rigid registration of reconstructed seed cloud to the known seed cloud. The average and standard deviation (STD) of localization error, defined as the distance between the true and reconstructed seeds, are shown in Fig. 7 for all the introduced pose errors. The average and STD of the matching rate are also shown in Fig. 7. The algorithm has an average matching rate of 99.2% when the pose error is zero.

As it can be seen in Fig. 7c–f, the algorithm shows consistently high matching rates and small localization errors over a wide range of errors along y_w and z_w as the C-arm motions in these two directions are compensated. Fig. 7a shows consistently high matching rates for errors of up to approximately 5 mm along x_w. However, the localization error increases monotonically with the error in this direction as shown in Fig. 7b. This is due to the fact that the matching problem is solved at the second level, using a 3D motion compensation; while we reconstruct the seeds using a 2D motion compensation at the third level. Therefore, the correct matching is found at the second level even in the presence of errors along x_w; however, the seed cloud is deformed at the third level, which leads to a monotonically increasing localization error. The matching and localization errors increase with the rotational pose errors, since the motion compensation algorithm does not compensate for rotational errors. However, the average matching rate is above 95% when rotational pose errors are less than 1.5°. We assume that in a clinical setting, the angles are measured with errors of less than ±1°.

3.2. Phantom study

We conducted a phantom study on a CIRS Model 053 tissue-equivalent prostate brachytherapy training phantom. An experienced brachytherapist inserted 26 needles to implant 136 dummy stranded seeds inside the phantom.

We took five images from the phantom using a GE OEC® 9800 mobile C-arm by rotation of the device around its PA in a 20° rotation span in approximately 5° intervals. A digital protractor was
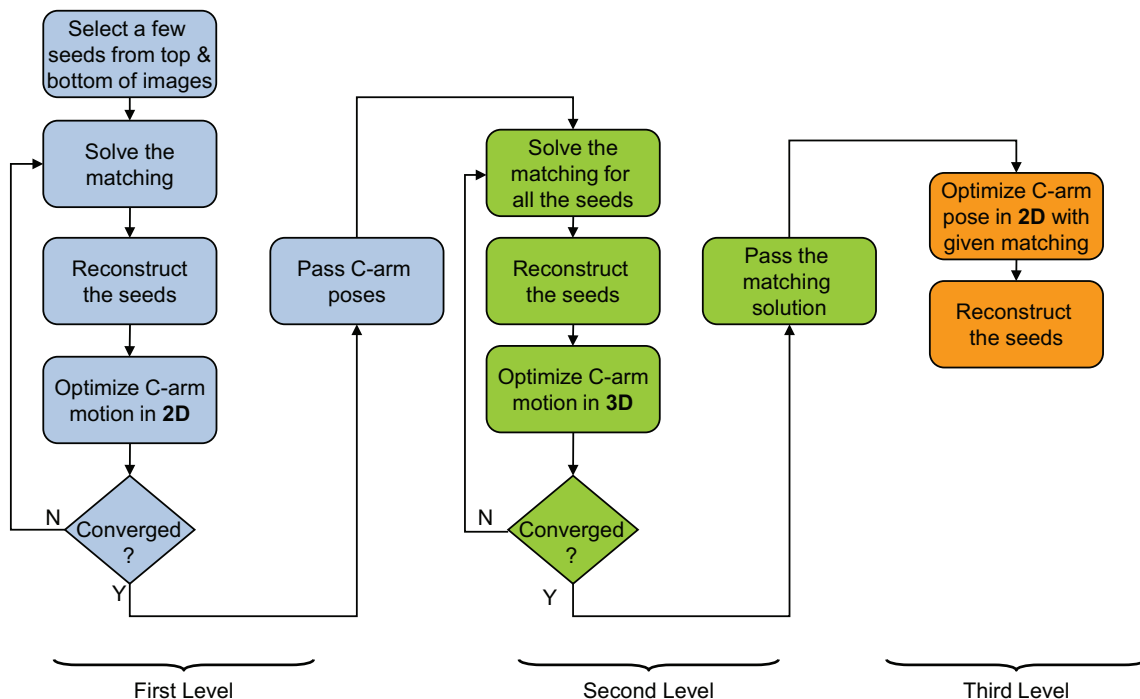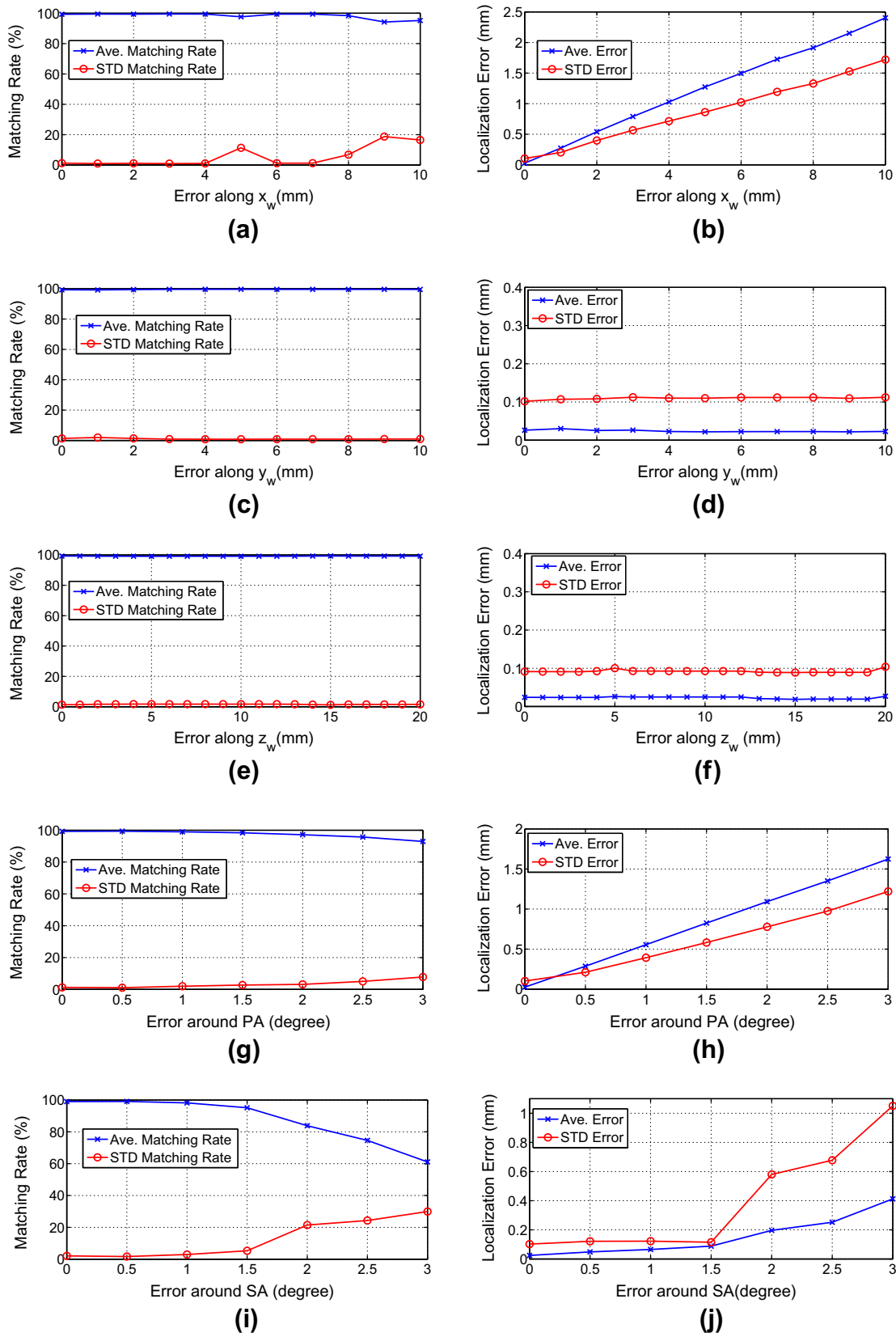

Fig. 6. The proposed three-level motion compensation algorithm.

Fig. 7. Simulation results, showing the average and standard deviation of matching rate and localization error for variable pose errors. The average and STD of matching rate for errors along x_w, y_w, z_w, PA and SA are shown in (a), (c), (e), (g) and (i), respectively. The average and STD of localization error for errors along x_w, y_w, z_w, PA and SA are shown in (b), (d), (f), (h) and (j), respectively.

connected to the source casing of the device to accurately measure the rotation angles. The seed projections were manually segmented in the images and the seeds were reconstructed in 3D using every combination of 3 out of 5 images (10 reconstructions) using motion compensation.

The phantom was also scanned using a Picker PQ5000 CT scanner. The seeds in the CT volume were segmented by thresholding and assumed as the ground truth. Although the CT and C-arm images were taken at different times, we assumed that the phantom deformation and seed displacements were negligible. We compared the seeds reconstructed from C-arm images to the seeds from CT after a rigid registration of the two seed clouds and reported the difference as localization error in Table 1.
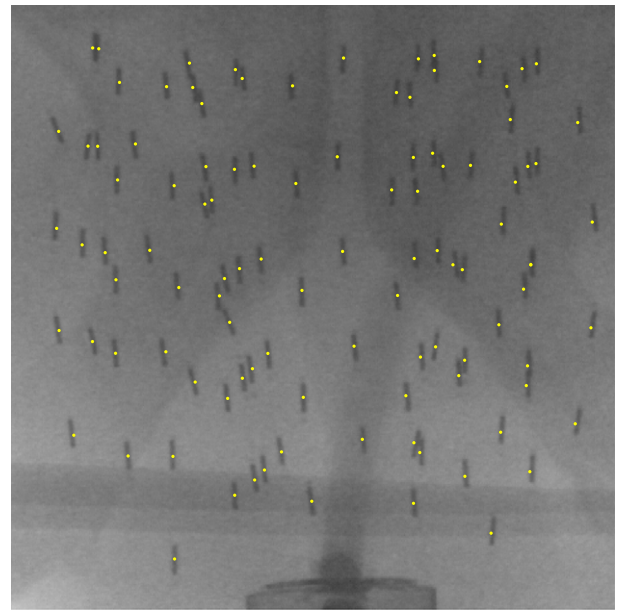
On average, we achieved a matching rate of 99.0% with 0.9 mm localization error. In order to show the importance of motion compensaion, we also tried to reconstruct the seeds without motion compensation and achieved an average of 78.3% for matching rate, which is far below the clinically acceptable level. Su et al. suggested that a seed detection rate of above 95% is required in order to achieve clinically sufficient estimation of dose distribution for contemporary ^{125}I prostate implants (Su et al., 2005).

3.3. Performance on clinical data

The performance of the motion compensation algorithm was also tested on clinical data. Ten patients were implanted with 100–135 ^{125}I seeds (average 112) at the British Columbia Cancer Agency. Five C-arm images were taken from each patient by rotation of the C-arm around the patient's craniocaudal axis at angles approximately 0°, ±5° and ±10°, while the SA angle was fixed. A GE OEC® 9800 mobile C-arm was used for imaging. This is a digital device with motorized joints. This device has a heavy intensifier that causes significant sagging and oscillation during image acquisition. For patients 1–8 the rotation angle around the PA was measured by a digital protractor which was attached to the source casing. The digital protractor did not interfere with the image of the anatomy or the working space and did not require precalibration. For the other 2 patients the rotation angles were measured using the joint encoders of the device. The digital protractor had a resolution of 0.1° while the device joint encoders had a resolution of 1°. We expect higher accuracy from the measurements of the protractor. The C-arm joint angle encoders showed a variation of 1° around the SA. This deviation was taken into account for initialization of the C-arm poses. The C-arm intrinsic parameters were once identified in a preoperative calibration and were assumed to be constant for all the rotation angles and all the patients. For each patient, we reconstructed the seeds for every combination of three images out of available five, thus obtaining 100 reconstructions in total. The seeds were manually segmented in the images. There were an average of 2 and maximum of 8 hidden seeds in the images.

Table 1
Matching rates and mean and standard deviation of localization error for phantom.

Rec. #	Matching rate (%)	Localization error mean ± STD (mm)
1	100.0	1.0 ± 0.6
2	100.0	0.9 ± 0.5
3	100.0	0.7 ± 0.4
4	99.2	0.9 ± 0.6
5	98.5	0.8 ± 0.4
6	98.5	0.8 ± 0.5
7	98.5	1.0 ± 0.6
8	98.5	0.8 ± 0.7
9	99.2	0.8 ± 0.4
10	97.8	0.9 ± 0.5

Fig. 8. Reprojected seeds overlaid on a C-arm fluoroscopy image, showing small projection errors.

The reconstructed seeds were reprojected on the images (see Fig. 8) and were meticulously inspected for matching errors. These images were also used to measure the projection error – defined as the distance between the segmented seed centroid and the projected location of the reconstructed seed - to quantify the reconstruction accuracy.
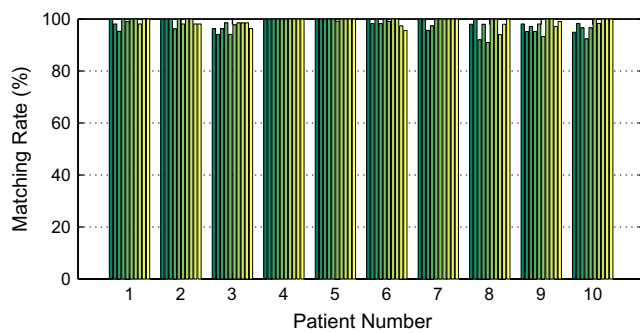
Fig. 9a shows the seed matching rate with motion compensation for each case. Overall, we achieved an average matching rate of 98.5% which is above the clinically accepted level. A perfect reconstruction was accomplished in 54% of the cases, while in 76% and 92% of the cases the matching rate was greater or equal to 98% and 95%, respectively.

In order to demonstrate the necessity of motion compensation, seed reconstruction was performed without motion compensation as well. As it can be seen in Fig. 9b, XMARSHAL without motion compensation achieved an average matching rate of 46.1%, which is a completely inadequate performance. Moreover, calculations show that motions of more than 30 mm in the up-down direction were compensated. This proves our hypothesis that it is necessary to use motion compensation, when only C-arm rotation angles are measured.
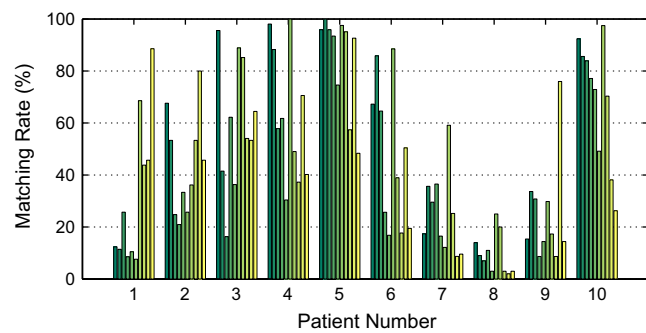
Fig. 9b directs us to another important role of the first-level optimization – other than increasing the speed. As it can be seen in Fig. 9b, an initial reconstruction without application of the first-level optimization can result in very unsuccessful matching results in which mismatched seeds are significantly abundant and can even outnumber the correctly matched seeds. In such cases, sole application of the second-level optimization can result in erroneous pose estimations since the large group of mismatched seeds can misguide the optimization algorithm. However, in the first-level optimization, the algorithm selects a handful of seeds from the top and bottom of the images that are very likely to correctly match. These few correctly matched seeds provide a good initial pose computation for the second level. Therefore, the first-level optimization not only shortens the computation time but also increases the robustness of the algorithm.

The mean and the standard deviation of the projection error are shown in Fig. 9c and d for correctly and erroneously matched seeds, respectively. The overall average and standard deviation of the projection error for correctly matched seeds are 0.33 mm and
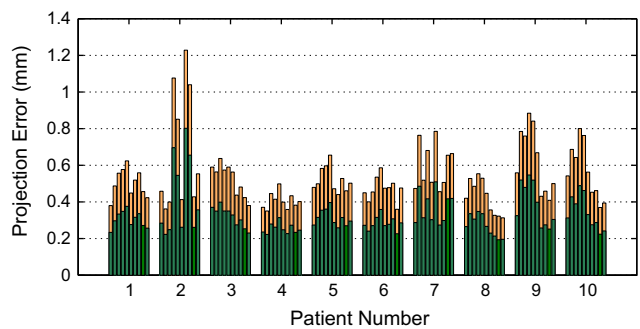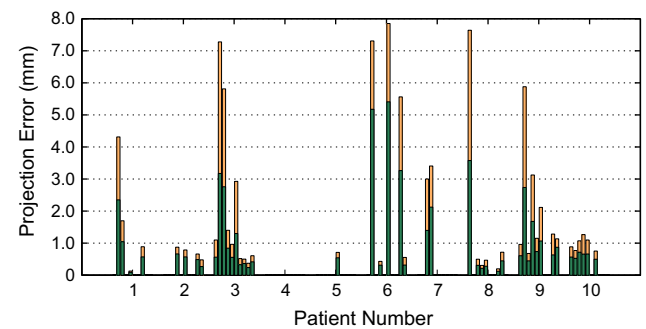
(a) Matching rate with motion compensation.

(b) Matching rate without motion compensation.

(c) Mean and STD of projection error for correctly matched seeds.

(d) Mean and STD of projection error for mismatched seeds.

Fig. 9. Clinical results showing the matching rate (a) with and (b) without motion compensation, the mean and STD of the projection error for (c) correctly and (d) erroneously matched seeds. In (c) and (d), the length of the green bars shows the mean, and the length of the orange bars shows the STD.

0.21 mm, respectively, which demonstrates high reconstruction accuracy. The mean and standard deviation of projection errors are 1.12 mm and 1.93 mm, respectively, for mismatched seeds.

It should be noted that the projection error cannot be used to measure the scaling factor. Therefore, we use seed spacing to provide additional confidence in our reconstruction accuracy. The patients in our study were implanted using stranded ^{125}I seeds. In such a case, the seeds that are implanted by a common needle are connected to each other by a bio-degradable strand that keeps them at a fixed center-to-center distance of 10 mm. We measured the center-to-center distances of the seeds that were inserted using a common needle and reported the results for each patient in Table 2. The overall seed spacing was 10.3 mm, which shows that significant scaling did not occur.

Table 2
The average and standard deviation of the distance between two consecutive seeds implanted by one needle.

Patient #	Seed spacing (mm) Mean ± STD
1	10.4 ± 0.6
2	10.4 ± 0.6
3	10.3 ± 0.4
4	10.3 ± 0.3
5	10.3 ± 0.3
6	10.2 ± 0.4
7	10.3 ± 0.4
8	10.1 ± 0.4
9	10.4 ± 0.5
10	10.3 ± 0.4
Overall	10.3 ± 0.5

4. Discussion

We achieved matching rates comparable to the results reported in Lee et al. (2009), Brunet-Benkhoucha et al. (2009), Lee et al. (2011). In particular, similar matching rates are reported in the original MARSHAL and XMARSHAL papers (Jain et al., 2005b; Kon et al., 2006). However, it should be noted that in all these works the C-arm pose was accurately known by using either a radio-opaque fiducial (Jain et al., 2005b; Kon et al., 2006; Lee et al., 2009; Lee et al., 2011) or a precisely calibrated and accurately tracked radiotherapy simulator in Brunet-Benkhoucha et al. (2009)(It should be noted that therapy simulators are extinct in contemporary radiation oncology). In other words, the C-arm was fully tracked and accurate poses were available. Due to availability of accurate C-arm poses in these works, motion compensation was not necessary. However, in our approach no external tracker was used to estimate the pose. Therefore, the initial pose recovery without motion compensation in our case was not sufficiently accurate for a

successful reconstruction (see Fig. 9b). However, with the proposed computational motion compensation method we achieved high matching rates without full pose tracking using any external tracker or fiducial (see Fig. 9a). This, in particular, explains the discrepancy between the successful results reported in Jain et al. (2005b), Kon et al. (2006) and our unsuccessful results with the same matching algorithm when motion compensation was not used.

In current brachytherapy practice, implant geometry is assessed using CT, one or several days after the procedure. However, the fluoroscopy images are taken at the end of the procedure while the patient is still in treatment position and additions to the implant are still possible to patch up cold spots. The prostate swells during and after the procedure which results in a seed displacement over time (Yamada et al., 2003) and even during the procedure (Jain et al., in press). The seeds also tend to migrate after

implantation (Fuller et al., 2004). Moreover, for our patients, the fluoroscopy images were taken while the ultrasound probe was still partially inside the rectum. The probe can deform the prostate and displace the seeds. Therefore, the physical position of the seeds during the CT scan is likely to be different from the position of the seeds when the C-arm images are taken. Hence, CT images of the patient can not be used as a confident ground truth to measure the localization error. Therefore, we relied on the projection error to validate the reconstruction in our clinical study. For the same reason, we had to rely on reprojected images to identify the mismatches. It was shown that seed localization errors of less than 2 mm result in less than 5% deviation in the prostate D90 (the minimum dose delivered to 90% of the prostate volume) (Lindsay et al., 2003; Su et al., 2007). Although it was not possible for us to measure the localization error in our clinical study, the localization errors in our simulations and phantom study were significantly lower than this threshold.

Although the mean and STD of the projection error for mismatched seeds are significantly larger than those of the correctly matched seeds (see Fig. 9c and d), the range of the projection error for correctly and erroneously matched seeds overlap. Therefore, a fixed threshold for the projection error cannot be used as a criterion to reliably detect the mismatches. However, it should be noted that, in some cases, a seed projection is mistakenly matched to a seed projection which is located very close to the correct one. In such cases, the projection error is small. Such mismatches result in small errors in seed localization. This suggests that if the seeds with large projection errors are removed, the rest of the mismatches may result only in an insignificant change in the dosimetry. Statistically, only 17.3% of mismatched seeds had a projection error larger than 2 mm. This is 0.2% of all the reconstructed seeds.

We used three C-arm images for seed reconstruction. While more could have been used, the fewer images used in the OR the better, primarily because it saves time and also reduces radiation exposure to OR staff. The matching rate is likely to improve by using more than three images at the expense of computational complexity (Kon et al., 2006). The motion compensation algorithm and the seed matching method are valid for an arbitrary number of images. Alternatively, seeds can be reconstructed for every combination of three out of all available images for a patient and the best reconstruction can be chosen. The reconstruction algorithm is sufficiently fast to allow for such a scheme in clinical settings. It should be noted that for all the patients, except patient 3, there is at least one reconstruction with perfect matching (see Fig. 9a).

The motion compensation algorithm can be combined with other seed matching algorithms, such as REDMAPS (Lee et al., 2011) as reported in Dehghan et al. (2010). In comparison to XMARSHAL, REDMAPS provides the optimal matching solution. Therefore, slightly better results – in term of matching rate – are expected. However, XMARSHAL is computationally faster than REDMAPS. Since, our matching rates using XMARSHAL are above the clinically acceptable threshold, we prefer XMARSHAL due to its speed.

In our results on clinical data, 8% of reconstructions have a matching rate of less than 95%. Although Su et al. suggested that a detection rate of at least 95% is required for an accurate dose estimation (Su et al., 2005), it should be noted that seed detection and matching rate are not completely equivalent. As mentioned above, many of the mismatches occur when a seed projection is mistakenly matched to a wrong seed projection, which is closely located to the correct seed projection. In this case the reconstructed seed is considered a mismatch but the localization error may be small. Therefore, all of the mismatched seeds cannot be categorized as undetected seeds. As explained, by using more than three images or employing a matching algorithm with optimal outcome such as REDMAPS (Lee et al., 2011), we can increase the matching rate.

We implemented our algorithm using MATLAB on a PC with an Intel 2.33 GHz Core2 Quad CPU and 3.25 GB of RAM. We achieved an average time of 19.4 s per data set, which is more than sufficient for clinical implementation. The first level of the optimization is very fast since only 10 seeds per image are used in the reconstruction and XMARSHAL runs on an $O(N^3)$ runtime. The second level of the algorithm is the most time consuming part, since a full matching problem must be solved at each iteration. However, using the outcomes of the first-level optimization to initialize the second level, significantly decreases the number of iterations necessary for convergence. We used the convergence of the reconstruction error as the stopping condition for the second level, which is a conservative criterion. As an alternative, the convergence of the matching solution can be used – similarly to the first-level optimization. In this case, if the matching solution does not change in two iterations, the optimization will terminate. This stopping condition is satisfied in significantly fewer iterations. However, it was observed during the simulations – although rarely - that a matching solution can change to a better one after three or more iterations. Since, the runtime for the algorithms is already acceptable, we decided to choose the more conservative criterion, in order to increase the seed matching rate. As mentioned before, the third-level optimization and seed reconstruction can be solved using (A.3) and (A.4) with low computational cost.

In our clinical studies, stranded seeds were used. We used the constant center-to-center distance of stranded seeds to show that no significant scaling occurred during motion compensation. It should be noted that our motion compensation and reconstruction algorithms do not rely on any information limited to stranded seeds and can be applied for loose seeds without algorithmic modifications.

In this work the seeds were manually segmented in the images by one observer without extensive efforts to identify all the hidden seeds. Since XMARSHAL is capable of maintaining above 97% matching rate for up to 1mm segmentation error (Kon et al., 2006), our motion compensated reconstruction method can successfully reconstruct the seeds as long as the manual seed segmentation error is below this threshold. Considering the small dimensions of seed projections, this level of accuracy is easily achievable. However, manual seed segmentation is a tedious task due to the large number of implanted seeds. Automatic seed segmentation methods are available that have a high success rate in identification of [125]I (Tubic et al., 2001b) or [103]Pd seeds (Kuo et al., 2010), even in the presence of overlapping seed projections. These methods can be used to segment the majority of seeds in the images. The missing seeds can be identified and the false positives can be removed with manual intervention. Integration of an automatic segmentation algorithm could facilitate the use of intraoperative dosimetry in a clinical environment.

We assumed that the C-arm rotates around its PA. This assumption – resulting in a horizontal motion of the seed projections in the images - was used in the first-level optimization to justify the selection of seeds from the top and bottom of every image as candidates for matching seeds. If the C-arm rotates around its SA, the seeds move vertically in the images. Therefore, the seeds that appear at the left or right side of one image are more likely to appear at the left or right side of other images. In this case, these seeds can be selected as candidates for matching seeds in the first-level optimization. Similarly to our case, the motion along the up-down direction, and perpendicular to the plane of rotation would be compensated.

Since we did not use radio-opaque fiducials, the C-arm could be positioned to capture the seeds close to the center of the detector. In this situation, the seed segmentation error caused by geometric distortion is below the tolerance level of XMARSHAL (Kon et al.,

2006). Therefore, we did not correct for the geometric distortion. If necessary, the dewarping parameters can be estimated using a single image captured at the center of the rotation span. Jain et al. showed that for small rotation spans, the dewarping parameters obtained from a center image can effectively correct the geometric distortions of all the images (Jain et al., 2007).

5. Conclusions and future work

We demonstrated that the sole measurement of rotation angles of a C-arm with a small angle span in a single plane, combined with a motion compensation algorithm, can result in successful prostate implant reconstruction. For motion compensation, we introduced a three-level optimization method to compensate for C-arm translational motions in the $Oy_w z_w$ plane using a small subset of seeds as fiducials to gain an initial estimate of the C-arm pose. This approach obviates the need full pose tracking with external trackers or fiducials.

In a clinical study of 100 data sets from 10 patients, an off-the-shelf digital protractor or C-arm joint encoders were used to measure the rotation angle around the PA of a C-arm, while the deviations in the angle around the left-right axis were measured using the C-arm joint encoders. Combined seed reconstruction and motion compensation led to on average seed matching rate of 98.5%, projection error of 0.33 mm and 19.8 s computational time. The high matching rate, insignificant scaling effect, low projection error and computation time show the feasibility of our method for intraoperative dosimetry in a clinical setting.

We assumed an insignificant motion of the C-arm along x_w axis. This assumption was validated by high matching rates and small projection errors in our clinical study. However, if on some C-arms this motion is considerably large, a 3D motion compensation is necessary. This, however, may suffer from the scaling problem. An object with a known length can be used to estimate the scale. Investigation on exploiting the length of ^{125}I seeds or seed spacers to recover the scaling factor is part of our future work.

Acknowledgements

Appendix A. Equations for simultaneous reconstruction and motion compensation

In order to find the optimal 2D offsets of M sources (M images) and at the same time, find the 3D position of N implanted seeds, we solve the following optimization problem.

$$(s_i^*, \delta_j^*) = \arg \min_{s,\delta} J \tag{A.1}$$

$$J = \sum_{i=1}^{N} \sum_{j=1}^{M} (s_i - q_j - \delta_j)' \left(I - v_{ij} v'_{ij} \right) (s_i - q_j - \delta_j), \tag{A.2}$$

where J is the total reconstruction cost, q_j is the initial position of jth source calculated form the joint angle readings, and δ_j is its corresponding offset. The minimality necessary conditions imply that:

$$\left[\sum_{j=1}^{M} V_{ij} \right] s_i - \sum_{j=1}^{M} V_{ij} \delta_j = \sum_{j=1}^{M} V_{ij} q_j, \tag{A.3}$$

$$- \sum_{i=1}^{N} V_{ij} s_i + \left[\sum_{i=1}^{N} V_{ij} \right] \delta_j = - \left[\sum_{i=1}^{N} V_{ij} \right] q_j, \tag{A.4}$$

where

$$V_{ij} = \left(I - v_{ij} v'_{ij} \right). \tag{A.5}$$

Eqs. (A.3) and (A.4) can be concatenated into a matrix form as below.

$$\mathbf{Ax} = \mathbf{b}, \tag{A.6}$$

$$\mathbf{x} = \begin{bmatrix} s'_1 & \cdots & s'_N & \delta'_1 & \cdots & \delta'_M \end{bmatrix}', \tag{A.7}$$

$$\mathbf{A} = \begin{bmatrix} A^{11}_{(3N \times 3N)} & A^{12}_{(3N \times 3M)} \\ A^{21}_{(3M \times 3N)} & A^{22}_{(3M \times 3M)} \end{bmatrix}, \tag{A.8}$$

$$\mathbf{b} = \begin{bmatrix} b'_1 & b'_2 \end{bmatrix}', \tag{A.9}$$

where,

$$A^{11} = \sum_{j=1}^{M} \left(\begin{bmatrix} V_{1j} & 0 & \cdots & 0 \\ 0 & V_{2j} & \cdots & 0 \\ 0 & 0 & \ddots & 0 \\ 0 & 0 & \cdots & V_{Nj} \end{bmatrix} \right), \tag{A.10}$$

$$A^{22} = \sum_{i=1}^{N} \left(\begin{bmatrix} V_{i1} & 0 & \cdots & 0 \\ 0 & V_{i2} & \cdots & 0 \\ 0 & 0 & \ddots & 0 \\ 0 & 0 & \cdots & V_{iM} \end{bmatrix} \right), \tag{A.11}$$

$$A^{12} = - \begin{bmatrix} V_{11} & \cdots & V_{1M} \\ V_{21} & \cdots & V_{2M} \\ \vdots & \ddots & \vdots \\ V_{N1} & \cdots & V_{NM} \end{bmatrix}, \tag{A.12}$$

$$A^{21} = (A^{12})', \tag{A.13}$$

$$b_1 = \sum_{j=1}^{M} \left(\begin{bmatrix} V_{1j} q_j \\ \vdots \\ V_{Nj} q_j \end{bmatrix} \right), \tag{A.14}$$

$$b_2 = - \sum_{i=1}^{N} \left(\begin{bmatrix} V_{i1} q_1 \\ \vdots \\ V_{iM} q_M \end{bmatrix} \right). \tag{A.15}$$

At this point, the set of linear equations in (A.6) is under-determined and the matrix $\mathbf{A}$ in (A.8) is singular. However, we fixed the first source in space; hence $\delta_1 = 0$. In addition, we assumed that the C-arms move only in $Oy_w z_w$ plane. This places another constraint on the equations in the form of $\delta_{jx} = 0$, $j \in \{1, \ldots, M\}$. By removing the rows and columns corresponding to these known variables from $\mathbf{A}$ and removing the corresponding entries in $\mathbf{x}$ and $\mathbf{b}$, Eq. (A.6) can be solved.

References

Amols, H.I., Rosen, I.I., 1981. A three-film technique for reconstruction of radioactive seed implants. Medical Physics 8, 210–214.

Blasko, J.C., Mate, T., Sylvester, J.E., Grimm, P.D., Cavanagh, W., 2002. Brachytherapy for carcinoma of the prostate: techniques, patient selection, and clinical outcomes. Seminars in Radiation Oncology 12 (1), 81–94. Advances in Brachytherapy.

Brack, C., Götte, H., Gossé, F., Moctezuma, J., Roth, M., Schweikard, A., 1996. Towards accurate X-ray camera calibration in computer-assisted robotic surgery. In: Proceedings of International Symposium on Computer Assisted Radiology, pp. 721–728.

Brunet-Benkhoucha, M., Verhaegen, F., Reniers, B., Lassalle, S., Béliveau-Nadeau, D., Donath, D., Taussky, D., Carrier, J.-F., 2009. Clinical implementation of a digital tomosynthesis-based seed reconstruction algorithm for intraoperative postimplant dose evaluation in low dose rate prostate brachytherapy. Medical Physics 36 (11), 5235–5244.

Dehghan, E., Lee, J., Moradi, M., Wen, X., Fichtinger, G., Salcudean, S.E., 2010. Prostate brachytherapy seed reconstruction using C-arm rotation measurement and motion compensation. In: Proceedings of Medical Image Computing and Computer Assisted Intervention (MICCAI), pp. 283–290.

Ding, M., Wei, Z., Gardi, L., Downey, D.B., Fenster, A., 2006. Needle and seed segmentation in intra-operative 3D ultrasound-guided prostate brachytherapy. Ultrasonics 44 (Suppl. 1), e331–e336, Proceedings of Ultrasonics International (UI'05) and World Congress on Ultrasonics (WCU).

Fallavollita, P., Karim-Aghaloo, Z., Burdette, E., Song, D., Abolmaesumi, P., Fichtinger, G., 2010. Registration between ultrasound and fluoroscopy or CT in prostate brachytherapy. Medical Physics 37, 2749–2760.

Feleppa, E.J., Ramachandran, S., Alam, S.K., Kalisz, A., Ketterling, J.A., Ennis, R.D., Wuu, C.-S., 2002. Novel methods of analyzing radio-frequency echo signals for the purpose of imaging brachytherapy seeds used to treat prostate cancer. In: Proceedings of SPIE, vol. 4687, pp. 127–138.

French, D.F., Morris, J., Keyes, M., Goksel, O., Salcudean, S.E., 2005. Intraoperative dosimetry for prostate brachytherapy from fused ultrasound and fluoroscopy images. Academic Radiology 12, 1262–1272.

Fuller, D.B., Koziol, J.A., Feng, A.C., 2004. Prostate brachytherapy seed migration and dosimetry: analysis of stranded sources and other potential predictive factors. Brachytherapy 3 (1), 10–19.

Grzeda, V., Fichtinger, G., 2010. C-arm rotation encoding with accelerometers. International Journal of Computer Assisted Radiology and Surgery 5 (4), 385–391.

Han, B.H., Wallner, K., Merrick, G., Butler, W., Sutlief, S., Sylvester, J., 2003. Prostate brachytherapy seed identification on post-implant TRUS images. Medical Physics 30 (5), 898–900.

Holmes III, D.R., Robb, R.A., 2004. Improved automated brachytherapy seed localization in trans-urethral ultrasound data. In: Galloway, R.L. (Ed.), Proceedings of SPIE, vol. 5367, pp. 353–360.

Jain, A., An, M., Chitphakdithai, N., Chintalapani, G., Fichtinger, G., 2007. C-arm calibration – is it really necessary? In: Cleary, K., Miga, M.I. (Eds.), Proceedings of SPIE, vol. 6509.

Jain, A., Deguet, A., Iordachita, I., Chintalapani, G., Vikal, S., Blevins, J., Le, Y., Armour, E., Burdette, C., Song, D., Fichtinger, G., in press. Intra-operative 3D guidance and edema detection in prostate brachytherapy using a non-isocentric C-arm. Medical Image Analysis, doi:10.1016/j.media.2010.07.011.

Jain, A., Fichtinger, G., 2006. C-arm tracking and reconstruction without an external tracker. In: Proceedings of Medical Image Computing and Computer Assisted Intervention (MICCAI), pp. 494–502.

Jain, A., Mustufa, T., Zhou, Y., Burdette, C., Chirikjian, G.S., Fichtinger, G., 2005a. FTRAC – a robust fluoroscope tracking fiducial. Medical Physics 32 (10), 3185–3198.

Jain, A.K., Zhou, Y., Mustufa, T., Burdette, E.C., Chirikjian, G.S., Fichtinger, G., 2005b. Matching and reconstruction of brachytherapy seeds using the Hungarian algorithm (MARSHAL). Medical Physics 32, 3475–3492.

Jemal, A., Siegel, R., Xu, J., Ward, E., 2010. Cancer statistics, 2010. CA: A Cancer Journal for Clinicians 60, 277–300.

Kon, R.C., Jain, A.K., Fichtinger, G., 2006. Hidden seed reconstruction from C-arm images in brachytherapy. In: IEEE International Symposium on Biomedical Imaging: Nano to Macro.

Kuo, N., Lee, J., Deguet, A., Song, D., Burdette, E.C., Prince, J., 2010. Automatic segmentation of seeds and fluoroscope tracking (FTRAC) fiducial in prostate brachytherapy X-ray images. In: Wong, K.H., Miga, M.I. (Eds.), Proceedings of SPIE, vol. 7625, pp. 76252T1–76252T9.

Lagerburg, V., Moerland, M.A., Lagendijk, J.J., Battermann, J.J., 2005. Measurement of prostate rotation during insertion of needles for brachytherapy. Radiotherapy and Oncology 77, 318–323.

Lam, S.T., Cho, P.S., Marks II, R.J., Narayanan, S., 2004. Three-dimensional seed reconstruction for prostate brachytherapy using Hough trajectories. Physics in Medicine and Biology 49, 557–569.

Lee, J., Labat, C., Jain, A.K., Song, D.Y., Burdette, E.C., Fichtinger, G., Prince, J.L., 2011. REDMAPS: reduced-dimensionality matching for prostate brachytherapy seed reconstruction. IEEE Transactions on Medical Imaging 30 (1), 38–51.

Lee, J., Liu, X., Jain, A., Song, D., Burdette, E., Prince, J., Fichtinger, G., 2009. Prostate brachytherapy seed reconstruction with Gaussian blurring and optimal coverage cost. IEEE Transactions on Medical Imaging 28 (12), 1955–1968.

Lindsay, P.E., Van Dyk, J., Battista, J.J., 2003. A systematic study of imaging uncertainties and their impact on ^{125}I prostate brachytherapy dose evaluation. Medical Physics 30 (7), 1897–1908.

McAleavey, S., Rubens, D., Parker, K., 2003. Doppler ultrasound imaging of magnetically vibrated brachytherapy seeds. IEEE Transactions on Biomedical Engineering 50 (2), 252–254.

Mitri, F., Trompette, P., Chapelon, J.-Y., 2004. Improving the use of vibro-acoustography for brachytherapy metal seed imaging: a feasibility study. IEEE Transactions on Medical Imaging 23 (1), 1–6.

Morris, W., Keyes, M., Palma, D., Spadinger, I., McKenzie, M., Agranovich, A., Pickles, T., Liu, M., Kwan, W., Wu, J., Berthelet, E., Pai, H., 2009a. Population-based study of biochemical and survival outcomes after permanent ^{125}I brachytherapy for low- and intermediate-risk prostate cancer. Urology 73 (4), 860–865.

Morris, W.J., Keyes, M., Palma, D., McKenzie, M., Spadinger, I., Agranovich, A., Pickles, T., Liu, M., Kwan, W., Wu, J., Lapointe, V., Berthelet, E., Pai, H., Harrison, R., Kwa, W., Bucci, J., Racz, V., Woods, R., 2009b. Evaluation of dosimetric parameters and disease response after ^{125}Iodine transperineal brachytherapy for low- and intermediate-risk prostate cancer. International Journal of Radiation Oncology, Biology, Physics 73 (5), 1432–1438.

Nag, S., Ciezki, J.P., Cormak, R., Doggett, S., Dewyngaert, K., Edmundson, G.K., Stock, R.G., Stone, N.N., Yan, Y., Zelefsky, M.J., 2001. Intraoperative planning and evaluation of permanent prostate brachytherapy: report of the American brachytherapy society. International Journal of Radiation Oncology, Biology, Physics 51, 1422–1430.

Narayanan, S., Cho, P.S., Marks II, R.J., 2004. Three-dimensional seed reconstruction from an incomplete data set for prostate brachytherapy. Physics in Medicine and Biology 49, 3483–3494.

Navab, N., Bani-Hashemi, A., Mitschke, M., Holdsworth, D.W., Fahrig, R., Fox, A.J., Graumann, R., 1996. Dynamic geometrical calibration for 3D cerebral angiography. SPIE Medical Imaging 2708, 361–370.

Orio III, P.F., Tutar, I.B., Narayanan, S., Arthurs, S., Cho, P.S., Kim, Y., Merrick, G., Wallner, K.E., 2007. Intraoperative ultrasound-fluoroscopy fusion can enhance prostate brachytherapy quality. International Journal of Radiation Oncology, Biology, Physics 69 (1), 302–307.

Peters, T., Cleary, K. (Eds.), 2008. Image-Guided Interventions: Technology and Applications. Springer.

Polo, A., Salembier, C., Venselaar, J., Hoskin, P., 2010. Review of intraoperative imaging and planning techniques in permanent seed prostate brachytherapy. Radiotherapy and Oncology 94 (1), 12–23.

Prestidge, B.R., Prete, J.J., Buchholz, T.A., Friedland, J.L., Stock, R.G., Grimm, P.D., Bice, W.S., 1998. A survey of current clinical practice of permanent prostate brachytherapy in the United States. International Journal of Radiation Oncology, Biology, Physics 40 (2), 461–465.

Song, D.Y., Jain, A.K., Zhang, Z., Deguet, A., Le, Y., Armour, E., Burdette, E.C., Fichtinger, G., 2011. Dynamic intraoperative dosimetry for prostate brachytherapy using a nonisocentric C-arm. Brachytherapy 10 (2), 98–106.

Su, Y., Davis, B.J., Furutani, K.M., Herman, M.G., Robb, R.A., 2007. Dosimetry accuracy as a function of seed localization uncertainty in permanent prostate brachytherapy: increased seed number correlates with less variability in prostate dosimetry. Physics in Medicine and Biology 52 (11), 3105–3119.

Su, Y., Davis, B.J., Herman, M.G., Manduca, A., Robb, R.A., 2005. Examination of dosimetry accuracy as a function of seed detection rate in permanent prostate brachytherapy. Medical Physics 32 (9), 3049–3056.

Su, Y., Davis, B.J., Herman, M.G., Robb, R.A., 2004. Prostate brachytherapy seed localization by analysis of multiple projections: identifying and addressing the seed overlap problem. Medical Physics 31 (5), 1277–1287.

Su, Y., Davis, B.J., Herman, M.G., Robb, R.A., 2006. TRUS-fluoroscopy fusion for intraoperative prostate brachytherapy dosimetry. In: Medicine Meets Virtual Reality 14: Accelerating Change in Healthcare: Next Medical Toolkit. Studies in Health Technology and Informatics, vol. 119/2005. IOS Press, pp. 532–537.

Todor, D.A., Cohen, G.N., Amols, H.I., Zaider, M., 2002. Operator-free, film-based 3D seed reconstruction in brachytherapy. Physics in Medicine and Biology 47, 2031–2048.

Tubic, D., Zaccarin, A., Beaulieu, L., Pouliot, J., 2001a. Automated seed detection and three-dimensional reconstruction. II. Reconstruction of permanent prostate implants using simulated annealing. Medical Physics 28 (11), 2272–2279.

Tubic, D., Zaccarin, A., Pouliot, J., Beaulieu, L., 2001b. Automated seed detection and three-dimensional reconstruction. I. Seed localization from fluoroscopic images or radiographs. Medical Physics 28 (11), 2265–2271.

Tutar, I.B., Gong, L., Narayanan, S., Pathak, S.D., Cho, P.S., Wallner, K., Kim, Y., 2008. Seed-based transrectal ultrasound-fluoroscopy registration method for intraoperative dosimetry analysis of prostate brachytherapy. Medical Physics 35, 840–848.

Tutar, I.B., Managuli, R., Shamdasani, V., Cho, P.S., Pathak, S.D., Kim, Y., 2003. Tomosynthesis-based localization of radioactive seeds in prostate brachytherapy. Medical Physics 30, 3135–3142.

Wei, Z., Gardi, L., Downey, D.B., Fenster, A., 2006. Automated localization of implanted seeds in 3D TRUS images used for prostate brachytherapy. Medical Physics 33 (7), 2404–2417.

Wen, X., Salcudean, S.E., Lawrence, P.D., 2010. Detection of brachytherapy seeds using 3D transrectal ultrasound. IEEE Transactions on Biomedical Engineering 57 (10), 2467–2477.

Yamada, Y., Potters, L., Zaider, M., Cohen, G., Venkatraman, E., Zelefsky, M.J., 2003. Impact of intraoperative edema during transperineal permanent prostate brachytherapy on computer-optimized and preimplant planning techniques. American Journal of Clinical Oncology 26, e130–e135.

Zhang, M., Zaider, M., Worman, M., Cohen, G., 2004. On the question of 3D seed reconstruction in prostate brachytherapy: the determination of X-ray source and film locations. Physics in Medicine and Biology 49, 19.